The influence of production mechanisms on pick-up ion loss at Mars

S. M. Curry,[1] M. Liemohn,[1] X. Fang,[2] Y. Ma,[3] and J. Espley[4]

[1]   This study quantifies the influence of ionization production mechanisms on ion escape and transport through near-Mars space. The Mars Test Particle simulation calculates the detailed ion velocity space distribution through a background magnetic and electric field model at specific locations. The main objective of this work is to extensively probe the sources of O^+ ion escape relative to the production mechanisms: photoionization, charge exchange, and electron impact. Seven production methods are explored and compared, resulting in total production and loss rates differing up to two orders of magnitude. Photoionization was compared as a function of solar zenith angle and optical shadow. Charge exchange O^+ production was studied with three methods: a constant rate assuming cold ion collisions, a constant rate proportional to the reaction cross-section and upstream solar wind bulk velocity, and finally a novel approach proportional to the cross-section and both the random and bulk velocity. Finally, electron impact ionization was considered as a constant and as a function of electron temperature. Of these methods, a baseline of the most physically relevant ion mechanisms was selected. Additionally, energy distributions at specific spatial locations highlight the individual ion populations in velocity space, revealing asymmetric and nongyrotropic features due to specific ionization methods. Analysis of the O^+ flux and loss is in agreement with observations and also indicates a strong polar plume in the northern hemisphere for a given interplanetary magnetic field orientation. We calculate the total production and escape to be 2.5×10^{25} and 6.4×10^{24}, respectively.

Citation: Curry, S. M., M. Liemohn, X. Fang, Y. Ma, and J. Espley (2013), The influence of production mechanisms on pick-up ion loss at Mars, *J. Geophys. Res. Space Physics*, *118*, 554–569, doi:10.1029/2012JA017665.

1. Introduction

[2]   Mars has undergone dynamic atmospheric evolution over the last billion years, particularly with respect to when and where water has existed. Geomorphic evidence of liquid water on the surface suggests that Mars must have had a much warmer, thicker atmosphere in order to provide the necessary pressure to sustain water in this state [*Squyres et al.*, 2004]. That atmosphere has evolved into a much colder and thinner atmosphere. While some of this water is frozen on or below the surface of Mars [*Carr*, 2003], a portion has escaped to deep space as neutral or charged particles. Consequently, studying the current atmospheric production and loss of oxygen and hydrogen addresses the bigger challenge of how the presence of water has evolved on Mars. Nonthermal atmospheric loss mechanisms play a significant role in this area, including pick-up ion processes [*Cravens et al.*, 2002; *Luhmann et al.*, 2006; *Fang et al.*, 2008], dissociative recombination of molecular ions [*Lammer and Bauer*, 1991; *Fox*, 1993], and atmospheric sputtering [*Luhmann and Kozyra*, 1991; *Johnson*, 1994]. Thermal loss processes (Jeans and hydrodynamic escape) and impact erosion [*Hunten*, 1993] are also important, but this paper will focus on the nonthermal aspects of pick-up ion escape.

[3]   Because Mars lacks an intrinsic dipole magnetic field, the solar wind directly interacts with the neutral atmosphere. Mars possesses an extended hot oxygen and hydrogen corona, which can be ionized and subsequently accelerated, or picked up, and swept away by the solar wind flow [*Luhmann and Kozyra*, 1991]. The convective electric fields and interplanetary magnetic fields (IMF) transfer momentum and energy to the newly created pickup ions, slowing the solar wind flow around the planet. The processes of pickup ions and mass loading on Mars represent the complex interaction between an unmagnetized planet and the solar wind and are a critical area of research in understanding atmospheric evolution.

[4]   Pick up ions are generated in both the ionosphere and exosphere in one of three ways. Through photoionization,

[1]Department of Atmospheric and Space Sciences, University of Michigan, Ann Arbor, Michigan, USA.
[2]University of Colorado, Laboratory for Atmospheric and Space Physics, Boulder, Colorado, USA.
[3]University of California, Institute of Geophysics and Planetary Physics, Los Angeles, California, USA.
[4]NASA Goddard Space Flight Center, Greenbelt, Maryland, USA.

Corresponding author: S. M. Curry, Department of Atmospheric and Space Sciences, University of Michigan, Ann Arbor, MI, USA. (smcurry@umich.edu)

solar radiation ionizes the planetary neutrals. Charge exchange collisions occur with both solar wind protons and planetary ions and finally, solar wind electrons impact and ionize neutrals. These pick-up ions constitute a major source of nonthermal atmospheric loss on Mars. The most abundant ion species in the Mars plasma environment are CO_2^+, O^+, H^+ and O_2^+. The approach for this paper focuses on quantifying O^+ loss and the contributing factors to O^+ escape in order to better understand the erosion of the Martian atmosphere. Specifically, this study uses a test particle approach to examine the relative contribution of different production mechanisms for upper atmospheric O + ions, which has not been explored in detail.

[5] Measurements from the Phobos 2, Mars Global Surveyor (MGS), and the Mars Express (MEX) missions have provided numerous observations of the pickup ion process and subsequent escape [*Lundin et al.*, 1989; *Rosenbauer et al.*, 1989; *Barabash et al.*, 1991; *Verigin et al.*, 1991; *Lundin et al.*, 2004; *Dubinin et al.*, 2006; *Fedorov et al.*, 2006; *Barabash et al.*, 2007; *Lundin et al.*, 2009]. *Barabash et al.* [2007] reported escape rates of 1.6×10^{23} for solar minimum from the ASPERA-3 ion mass analyzer instrument on board the MEX spacecraft, showing agreement with a number of modeled results [*Ma et al.*, 2004; *Modolo et al.*, 2005; *Chaufray et al.*, 2007; *Terada et al.*, 2009; *Kallio et al.*, 2010; *Najib et al.*, 2011] . Using a different mode of the MEX ion mass analyzer, *Lundin et al.* [2009] extended the energy range of the *Barabash et al.* [2007] study and consequently increased the observed loss rate by an order of magnitude to 2.1×10^{24}.

[6] In addition to observations, various models and observational studies have also addressed pick up ions in the broader context of Martian atmospheric evolution. In investigating the solar wind's interaction with Mars, simulations have been extremely useful tools for probing the physics of this system. Generally, they fall into three categories: MHD models [*Liu et al.*, 1999; *Ma et al.*, 2004; *Harnett and Winglee*, 2006; *Jin et al.*, 2006; *Terada et al.*, 2009; *Najib et al.*, 2011], hybrid models [*Modolo et al.*, 2005; *Boesswetter et al.*, 2007; *Kallio et al.*, 2010; *Brecht and Ledvina*, 2010; *Kallio and Jarvinen*, 2012; *McKenna et al.*, 2012], and test particle simulations [*Luhmann and Kozyra*, 1991; *Kallio and Koskinen*, 1999; *Cravens et al.*, 2002; *Luhmann et al.*, 2006; *Fang et al.*, 2008].

[7] MHD models describe the plasma environment as a fluid, and therefore are very efficient at self-consistently solving for the plasma parameters and magnetic field configuration around a planet. However, they assume a Maxwellian velocity distribution, and as a consequence, do not account for pickup ions with extremely large gyroradii [*Liu et al.*, 1999; *Ma et al.*, 2004; *Harnett and Winglee*, 2006; *Terada et al.*, 2009; *Najib et al.*, 2011]. Hybrid models represent the ions as individual particles and the electrons as a massless charged neutralizing fluid, but can be computationally taxing. As a consequence, the number of particles per cell above 300 km is very limited on the order of 5 to 30 [*Brecht and Ledvina*, 2006; *Modolo et al.*, 2005; *Boesswetter et al.*, 2007; *Kallio et al.*, 2010]. It should be noted that *Brecht and Ledvina* [2010] used 16–20 particles per cell in the shock region but launched 10,000 particles per cell in the ionosphere. While self-consistent models are important for predicting plasma parameters, test-particle

simulations have the capability to resolve the distribution of ions in velocity space using billions of particles, which can reveal features about ion trajectories and subsequent loss. Because the constraints of a Maxwellian approach are lifted, there is no averaging of gyroradii or pitch angles, which proves critical on an unmagnetized planet with gyroradii on planetary scales [*Luhmann and Kozyra*, 1991; *Kallio and Koskinen*, 1999; *Cravens et al.*, 2002; *Luhmann et al.*, 2006; *Fang et al.*, 2008; *Andersson et al.*, 2010; *Fang et al.*, 2010].

[8] A study by *Brain et al.* [2010] compared seven models in order to investigate the Mars electromagnetic environment, including O^+ escape rates. Using identical inputs for the solar wind, neutral atmosphere, ionosphere, IMF, and EUV, over an order of magnitude difference for the O^+ escape rates existed among the models. The strong variations in the modeled atmospheric escape and the observations are a critical motivation for probing the factors influencing how O^+ loss is calculated in the Mars space environment.

[9] Given the disparities in O^+ loss from observations and modeling efforts, this paper aims to investigate loss via the influence of O^+ ion production processes: photoionization, electron impact and charge exchange. Similar studies include *Zhang et al.* [1993] and *Bauske et al.* [1998], who explored ion production at Mars and Venus respectively but did not examine the influence of ion production mechanisms on total escape rates or velocity space. While *Li et al.* [2011] did explore O^+ velocity space using a test particle model, the objective was the influence of crustal fields on the spatial and energy distribution of precipitating pickup ions. Because the MTP can be run with over 10^9 particles, pickup ion distributions in velocity space are finely resolved and therefore can be used to describe specific populations of escaping O^+ [*Fang et al.*, 2008]. The MTP simulation is based on the published model of *Fang et al.* [2008] and uses background MHD electromagnetic fields from *Ma et al.* [2004].

[10] Section 2 discusses the specific inputs and assumptions of both the MHD and MTP simulations. Section 3 discusses a comparison of O^+ production methods and proposes a baseline of the most physically representative methods given the assumptions of the MTP simulation. Section 4 outlines the results from pickup ion distributions in velocity space run with over 10^9 particles, describing specific populations of escaping O^+ and their origins. Section 5 examines spatial distributions of escape particularly in the downtail and polar locations and presents a table of total production and escape rates for each method. Section 6 discusses the approach and the results along with a review of the assumptions of the MTP simulation. Finally, Section 7 summarizes and concludes this study.

2. Approach

[11] The Mars Test Particle (MTP) simulation is a test particle simulation that launches and tracks particles through the Mars space environment. The propagation of ions is governed by the Lorentz force [*Fang et al.*, 2008], where the background magnetic and electric fields that the ions follow are calculated by a separate MHD model from *Ma et al.* [2004]. The simulation follows the test particle trajectories by solving the Newton-Lorentz equation, obtaining a global

picture of the angular distributions and energy spectra of pickup oxygen ions in the Martian plasma environment. The test particle approach is valid if changes in the densities and pressure from the test particles are small compared to the MHD densities used to generate the background electric and magnetic fields. A cross check of densities throughout the MTP simulation and MHD simulation show agreement and while the MTP calculated O^+ densities are higher in some spatial locations, the MTP O^+ density is consistent with or less than the total MHD ion density.

2.1. MHD Model

[12] Because the test particle simulation does not self consistently calculate the magnetic and convective electric fields, background fields from the three-dimensional, multispecies MHD model of *Ma et al.* [2004] are used. Omitting the Hall terms, the convective electric field is calculated by:

$$\mathbf{E} = -\mathbf{U} \times \mathbf{B} \qquad (1)$$

where $\mathbf{U}$ is the bulk flow velocity and $\mathbf{B}$ is the magnetic field. The MHD simulation solves the dimensionless conservative form of the MHD equations for the field parameters in the plasma environment around Mars using a sophisticated, second-order accurate, numerical scheme [*Powell et al.*, 1999]. The simulation domain begins from a lower boundary in the ionosphere at 100 km and reaches an outer boundary beyond the bow shock at 8 R_M upstream and 24 R_M downstream. The code uses a spherical grid structure with vertical cell sizes of 10 km near the planet that logarithmically increases with radial distance in order to capture the ionospheric profile. By solving for multiple continuity equations and combined single momentum and energy equations, separate solutions for the mass densities of H^+, O^+, O_2^+, and CO_2^+ are resolved. Combined with a broad chemistry scheme, the ionospheric profile of *Ma et al.* [2004] shows strong agreement with MGS and Viking observations. Note that the model is able to capture plasma flows around the planet including ionospheric altitudes.

[13] The parameters used in this study are from Case 1 of *Ma et al.* [2004], which corresponds to a solar maximum condition. The IMF has a value of 3 nT using the Parker spiral structure in the *XY* plane at an angle of 56° and the solar wind velocity and density were set at 400 km/s and 4 cm^{-3}. A critical aspect of the induced magnetosphere at Mars is the effect of the crustal fields. These regions were first observed [*Acuna et al.*, 1999] by MGS and create a shielding effect that nonmagnetized planets and moons do not exhibit, thus changing the dynamics of the atmospheric evolution and erosion. The *Ma et al.* [2004] Case 1 simulation includes the crustal fields by implementing the 60° spherical harmonic scheme from *Arkani-Hamed* [2001] and positioned the strong crustal field region (roughly centered at 180°W) to be facing the Sun. *Ma et al.* [2004] illustrated that both the ion densities at high altitudes and the bow shock location are affected by the presence of the crustal fields. *Fang et al.* [2010] further exemplified this by varying the position of the crustal fields and finding the tailward escape rates changing by a factor of two (higher in the absence of crustal fields), consistent with *Ma and Nagy* [2007].

2.2. Mars Test Particle Simulation

[14] The MTP simulation was originally described in much detail by *Fang et al.* [2008]. It is a three-dimensional Monte Carlo model that randomly assigns the particles' initial position, energy, and direction. The simulation begins by launching 4.5 billion particles, 15,000 particles per source cell, time independently and using a Maxwellian energy distribution based on the neutral temperature and isotropic angular distribution. *Fang et al.* [2008] demonstrated that while the escape rate converges with only 10 or 100 particles per source cell, the velocity space resolution requires far more particles per cell (i.e., thousands) in accordance with the central limit theorem—the relative error in counting statistics is proportional to one over the square root of the number of counts. For a particle code result, this places a numerical error value on any calculated quantity. To achieve density within 10% accuracy, the grid cell requires 100 particles contributing to this quantity. If the grid cell only has 10 particles, then the numerical accuracy is known to only 30%. This error estimate is true in velocity space as well; to resolve the small-scale features of velocity space, then each grid cell needs many particles in regions of interest in velocity space. This is where a test particle simulation is well suited—following a large number of particles through a given field to better resolve small-scale features.

[15] After the particles are launched, the particles are considered collisionless due to the inner boundary being above the Martian exobase, which was estimated to be 220 km altitude during solar maximum conditions and above the peak of the ionosphere estimated at 140–150 km [*Lichtenegger et al.*, 2007]. Loss sources due to collisions of ions with the ambient neutrals are subsequently assumed to be negligible. Each particle is accelerated by the background electric and magnetic field and travels until it reaches the inner boundary of 300 km or the outer boundary of 3 R_M where the positions and trajectories are recorded. A sophisticated parallelization scheme was developed by *Fang et al.* [2008] in order to support the taxing computational requirements. Each particle carries a weight determined by the total ion production per cell divided by the total number of test particles per unit time [*Fang et al.*, 2008]. The trajectory is determined by solving Newton's equation of motion where the pick-up ion transport is dictated by the Lorentz force. It is important to note that the simulation tracks the full angular distribution of the particles, with no implicit averaging of the gyration or pitch angle of the particles. When the particles' trajectory and velocity are recorded, velocity space distributions can be constructed by assuming a virtual detector that observes the angular distribution and energy of the ions at any specified location within the simulation domain. For this study, the virtual detectors have been uniformly placed around the planet at different radial locations.
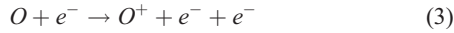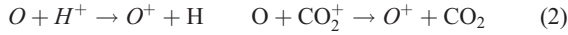
[16] The MTP simulation grid is spherical and uses cells with 5° by 5° resolution and logarithmic grid spacing with respect to radial distance [*Fang et al.*, 2008]. A Cartesian coordinate system corresponding to the Mars Solar Orbital scheme (MSO) is adopted where the system is centered at Mars and X_{MSO} points toward the Sun, Y_{MSO} is aligned with the dusk direction and Z_{MSO} completes the right hand system. Because the IMF is a Parker spiral in the ecliptic plane away from the Sun, the MSO and MSE (where Z_{MSE}

is aligned with the interplanetary electric field) coordinate systems are equivalent in this case. The neutral atmosphere in the simulation is spherically symmetric and constructed using the parameters from *Bougher and Engel* [2000] where H, O, and CO_2 dioxide were the main constituents. The hydrogen densities were based on rates from *Fox* [2003] and the temperature-dependent oxygen densities used the calculations of *Kim et al.* [1998]. Additional CO_2 densities at solar maximum were based on model results of *Bougher and Engel* [2000] and Mariner 6 and 7 observations [*Ma et al.*, 2004].

3. Ion Production

3.1. Methods

[17] In the equation of motion for the O^+ particle trajectories, singly ionized ions are assumed. The three dominant ionization mechanisms included in this study are photoionization of the upper neutral atmosphere, charge exchange with other ions, and electron impact from solar wind electrons:

$$O + hv \rightarrow O^+ + e^- \tag{1}$$

$$O + H^+ \rightarrow O^+ + H \qquad O + CO_2^+ \rightarrow O^+ + CO_2 \tag{2}$$

$$O + e^- \rightarrow O^+ + e^- + e^- \tag{3}$$

[18] We examine seven different methods for implementing these types of O^+ ionization, listed in Table 1 (please refer to the number in the table for each method in the descriptions below). These methods were selected in order to compare approaches used among numerous models including (but not limited to) *Stebbings et al.* [1964], *Zhang et al.* [1993], *Bauske et al.* [1998], *Ma et al.* [2004], *Modolo et al.* [2005], *Brecht and Ledvina* [2006], *Fang et al.* [2008], *Kaneda et al.* [2009], *Terada et al.* [2009], *Brain et al.* [2010], and *Najib et al.* [2011]. We consider the assumptions of each of these methods in relation to the MTP simulation and will propose the most physically sound methods for photoionization, charge exchange, and electron impact as a baseline. In particular, we assess the assumptions of ionization at high altitudes with regard to optical attenuation, the role of the extended corona interacting with the solar

wind protons, and temperature gradients at low versus high altitudes. In addition to evaluating ionization approaches used in other models, we also introduce novel approaches for photoionization (method 2) and charge exchange (method 5) in order to capture more realistic physical representations of ionization at high altitudes.

[19] For the O^+ photoionization rate of production, two methods are compared. Method (1) of Table 1 defines the reaction rate as a function of solar zenith angle (SZA) where the optical depth (τ) and attenuation (f_1) are determined by equation (6)

$$\tau = \frac{\sum_n \rho_n(z)\sigma_n H_n}{cos(SZA)}$$

$$f_1 = \begin{cases} e^{-\tau} & \text{if } SZA \leq 90° \text{ (in front of the terminator)} \\ 0 & \text{if } SZA > 90° \text{(behind the terminator)} \end{cases}$$

$$(4)$$

where ρ is the atmospheric density, σ is the cross-section and H is the scale height for n^{th} species used (CO_2, O, H). In the equatorial plane, the attenuation would simply be a function of altitude in front of the terminator plane (closest to the Sun) and would include the additional SZA attenuation behind the terminator plane, as seen in Figure 1a. This method is consistent with *Ma et al.* [2004], the model that supplies the background electric and magnetic fields, as well as many other models. Although this assumption is valid at lower altitudes, Figure 1a illustrates a sharp production difference at the terminator plane.

[20] The second method (2) for O^+ photoionization in Table 1 eliminates the solar zenith angle dependence and uses a constant reaction rate except in the cylindrical (geometrical) optical shadow behind the planet, as seen in equation (5). This method eliminates the solar zenith angle dependence because the simulation has a lower boundary of 300 km where the atmosphere is already optically thin, as seen in Figure 1b. As a point of reference, the optical depth (τ) at the inner boundary 300 km above the surface in the terminator plane and subsolar point is 6.5×10^{-3} and 3.2×10^{-6}, respectively. At 3 R_M, the corresponding values for τ are 4.6×10^{-4} and 2.3×10^{-7}. As discussed earlier, this is a novel method and the authors encourage other modelers to assess their

Table 1. Chemical Reaction Rates.

#	Method	Chemical Reaction	Rate Coefficient	Reference
1	Photoionization	$O + hv \rightarrow O^+ + e$	$k_1 = (2.73 \times 10^{-7})f_1$	*Schunk and Nagy* [2000][a]
2	Photoionization	$O + hv \rightarrow O^+ + e$	$k_2 = (2.73 \times 10^{-7})f_2$	Current approach[b]
3	Charge exchange	$H^+ + O \rightarrow H + O^+$	$k_3 = 5.08 \times 10^{-10}$	*Fox and Sung* [2001][c]
4	Charge exchange	$H^+ + O \rightarrow H + O^+$	$k_4 = v_{SW} \times 10^{-15}$	*Stebbings et al.* [1964][d]
5	Charge exchange	$H^+ + O \rightarrow H + O^+$	$k_5 = v_{total} \times 10^{-15}$	Current approach[e]
*	Charge exchange	$CO_2^+ + O \rightarrow CO_2 + O^+$	$k_* = 9.60 \times 10^{-11}$	*Schunk and Nagy* [2000]
6	Electron impact	$O + e \rightarrow O^+ + e + e$	$k_6 = 1.29 \times 10^{-8}$	*Cravens et al.* [1987][f]
7	Electron impact	$O + e \rightarrow O^+ + e + e$	$k_7 =$ table lookup	*Cravens et al.* [1987][g]

[a]Photoionization using solar zenith angle, s^{-1}.
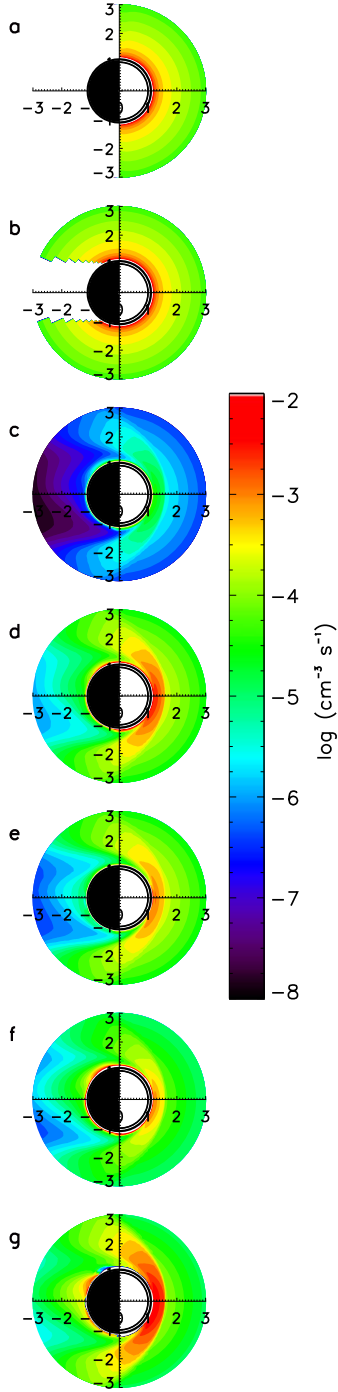[b]Photoionization using an optical shadow, s^{-1}.
[c]Charge exchange constant used by *Ma et al.* [2004] (cold H^+ + O), $cm^3 s^{-1}$.
[d]Charge exchange constant used by *Stebbings et al.* [1964] with bulk velocity (hot H^+ + O), $cm^3 s^{-1}$.
[e]Charge exchange using bulk and random velocity (hot H^+ + O), $cm^3 s^{-1}$.
[f]Electron impact using constant temperature of 1.5×10^5 K, $cm^3 s^{-1}$.
[g]Electron impact using calculated electron temperature per cell, $cm^3 s^{-1}$.

Figure 1. The equatorial view of the production rate shows seven sources of ionization from 300 km to 3 R_M in units of # $cm^{-3} s^{-1}$. The production schemes are as follows: (a) photoionization using SZA, (b) photoionization using optical shadow, (c) charge exchange using *Ma et al.* [2004] constant (cold H^+ + O), (d) charge exchange constant from *Stebbings et al.* [1964] using upstream bulk velocity (hot H^+ + O), (e) charge exchange using bulk and random velocity (hot H^+ + O), (f) electron impact using constant temperature of 1.5×10^5 K, (g) electron impact using electron temperature calculated per cell. See Figure 2 for a comparison of the low altitude region for Figures 1f and 1g. The color bar uses a log scale from 10^{-8} to 10^{-2}. It should be noted that the empty regions in are an area of zero production.

assumptions of optical attenuation and incorporate photoionization using an optical shadow at high altitudes.

$$f_2 = \begin{cases} 0 & \text{if } y^2 + z^2 < 1 \text{ and } x < 0 \\ 1 & \text{elsewhere} \end{cases} \quad (5)$$

[21] The O^+ charge exchange production rate is explored with methods 3, 4, and 5 of Table 1. Note the k_* charge exchange rate is the cold CO_2^+ production with neutral O but is not being modified in this study. The CO_2^+ reaction is simply added to each of the solar wind H^+ charge exchange methods (3, 4, 5) when describing the total charge exchange production or loss. Both the CO_2^+ and H^+ densities are provided by the *Ma et al.* [2004] simulation, which provides the background electric and magnetic fields for the MTP simulation.

[22] Method (3) is consistent with a constant reaction rate from *Ma et al.* [2004] (originally described in *Fox and Sung* [2001]). This rate describes the interaction of cold ions and neutrals and does not account for charge exchange in the extended oxygen corona with the hot solar wind protons. As seen in Figure 1c, this O^+ charge exchange production rate produces very little O^+ beyond 2 R_M.

[23] The O^+ charge exchange method (4) of Table 1 is a bulk velocity based constant reaction rate consistent with *Stebbings et al.* [1964]. The reaction rate can be described by multiplying the $H^+ - O$ cross-section by the bulk velocity as seen in equation (8). Thus, the extended oxygen corona is ionized as a function of bulk velocity, seen in Figure 1d. The much higher rate of O^+ production is clear at the higher altitudes of 2 to 3 R_M where the hot solar wind protons ionize the corona (hot energetic charge exchange).

$$k_4 = v_{SW} \times 10^{-15}$$
$$= 4.00 \times 10^{-8} (cm^3 \ sec^{-1}) \quad (6)$$

[24] The final charge exchange process, described in method (5) in Table 1, accounts for the hot solar wind protons interacting with the oxygen corona as well as the dissipated energy within the induced magnetosheath. The neutrals in the corona will experience hot energetic charge exchange with the solar wind protons, but the velocity of the solar wind is no longer a constant. Because the bulk velocity transitions from supersonic to subsonic, energy is dissipated as the solar wind approaches the planetary obstacle and is transferred to the particles random velocity. The reaction rate can now be described by multiplying the $H^+ - O$ cross-section by the total velocity in each cell, where the total velocity is the bulk velocity plus the random velocity, as seen in equation (9). This approach has not been published in this context and is an important scheme to consider for future modeling work. The reaction rate is defined as follows:

$$v_{random} = \sqrt{\frac{2kT_i}{m}}$$
$$v_{bulk} = \sqrt{U_x^2 + U_y^2 + U_z^2} \quad (7)$$
$$v_{total} = \sqrt{v_{random}^2 + v_{bulk}^2}$$
$$k_5 = v_{total} \times 10^{-15} (cm^2)$$

where it is assumed that $T_i = T_e$ from the MHD results. Figure 1e illustrates the lower O^+ production as a result of

the lower total velocity at the shock and in the wake of the planet. In the other two methods of charge exchange (3 and 4), the use of a constant reaction rate could overestimate or underestimate the ionization in certain locations. It should be noted that additional charge exchange rates from *Jin et al.* [2006] are based on $T_n = 1000$ K and fall in between the k_3 and k_4 constants but were not included in this study.

[25] Finally, the ionization due to the solar wind electron impact is explored with methods (6) and (7) from Table 1. Method (6) corresponds to a constant electron impact rate based on $T_e = 1.5 \times 10^5$ K, a rate that other models have assumed and a value that is reasonable for the solar wind and magnetosheath regions around Mars. The last electron impact ionization method (7) uses electron temperature dependence with rates based on the schema for O^+ impact ionization from *Cravens et al.* [1987]. Figure 1f illustrates generally higher O^+ production than in 1 g due to the average electron temperature being an order of magnitude higher ($\sim 10^6$ K) *except* at lower altitudes. It is critical to compare the electron temperature at low altitudes because the neutral density is much higher, which drastically changes the total O^+ production.

[26] Figure 2 compares the electron impaction ionization with and without temperature dependence at 9 P.M. local time (method 6 and 7 respectively). Figure 2a plots the electron temperature on the left y-axis in blue and the corresponding electron impact rate on the right y-axis in green as a function of altitude. Below 1.4 R_M, the simulated electron temperature drops three orders of magnitude, as seen by the solid navy line. The corresponding reaction rate, the green solid line, also drops with electron temperature. However, using a constant electron temperature creates a constant reaction rate which grossly overestimates the ionization at low altitudes as seen by the dashed navy and green lines respectively. Figure 2b plots the O^+ production rate on the left axis in black and the neutral profile of atomic oxygen in red on the right as a function of altitude. Because O^+ production is a product of the neutral density and the reaction rate (k), two very different scenarios arise below 1.4 R_M. When the constant reaction rate (dashed green line above in Figure 2a) is applied to the neutral density (solid red line), the O^+ production is six orders of magnitude larger, as seen in the dashed black line. In the case of the simulated electron temperature, the lower ionization rate (solid green line in Figure 2a) due to the lower temperature is applied, resulting in lower production. Method 7 is much more physically accurate in that the electron density from the solar wind is not going to be constant throughout the magnetosheath and will decrease toward the planet. With fewer electrons, there will be less electron impact ionization. Subsequently, temperature-dependent electron reaction rates critically affect the total production and loss, which will be discussed again in the results section.

[27] From the seven methods outlined in Table 1, three have been selected as a baseline due to their consistency with the physical assumptions of the MTP simulation. The ionization methods begin with assessing photoionization as a function of solar zenith angle (method 1) and optical shadow (method 2). This study focuses on high altitudes, above 300 km, where the optical attenuation is negligibly small so using the photoionization method with just the optical shadow, method (2) is adopted for the baseline. Next, the charge exchange methods were explored using a constant reaction rate for the cold ions and neutrals consistent
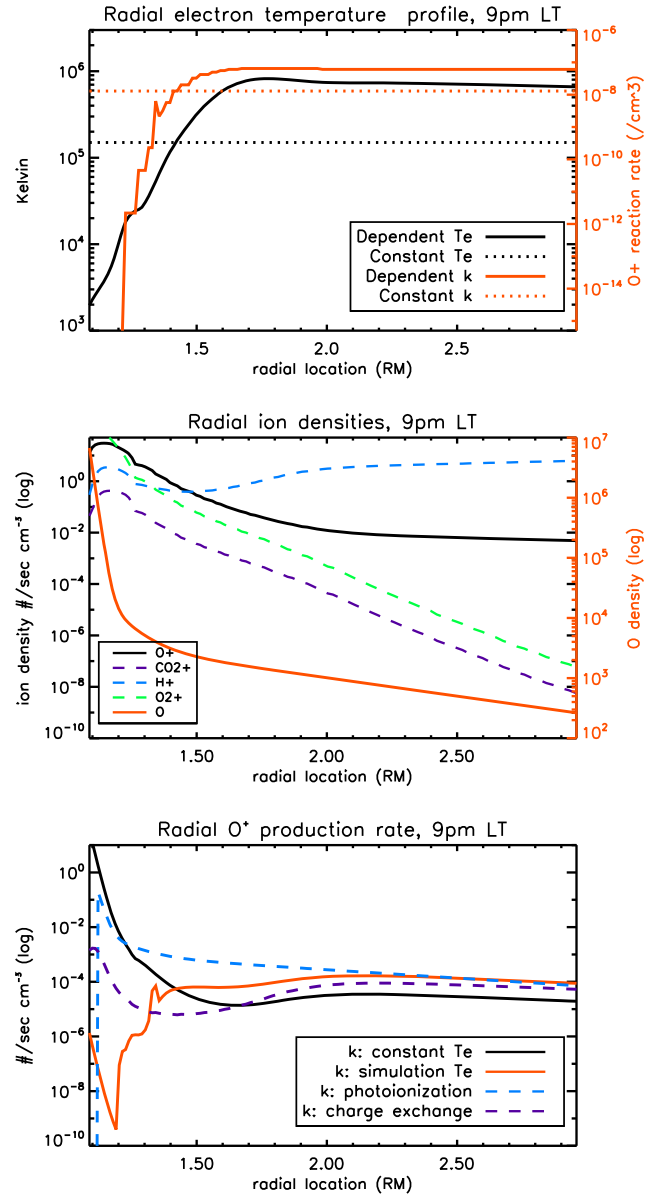
Figure 2. A radial slice at 9 pm local time illustrates the reaction rates for electron impact ionization with a constant electron temperature of 1.5×10^5 K and a temperature-dependent rate (methods 6 and 7, respectively). (a) Radial profile of the electron temperature (left axis) and reaction rate (right axis) where the solid navy and green lines represent the simulated electron temperature and corresponding reaction rate, respectively. The dotted navy and green lines represent a constant temperature and corresponding reaction rate respectively. (b) O^+ production rates for methods 6 and 7 on the left axis and the neutral O density in red on the right axis. Below 1.3 R_M, note the difference in O^+ production due to the high neutral O density. The simulated reaction rate, solid black line, is over five orders of magnitude higher than the constant reaction rate, dashed black line.

with *Ma et al.* [2004] (method 3—recall this is the MHD model, which provides the background electric and magnetic fields), a rate using the bulk velocity to account for the hot ions interacting with the corona [*Stebbings et al.*, 1964]

(method 4) and a novel approach using bulk and random velocity to account for the hot ions interacting with the corona (method 5). Because the bulk velocity is not representative of the total velocity, especially at low altitudes, the novel method 5 is adopted for the baseline. Finally, the study compares electron impact ionization with and without temperature dependence. As discussed in Figure 2, assuming a constant electron temperature in method 6 grossly overestimates the O^+ production rate for below 1.4 R_M. Subsequently temperature-dependent electron impact ionization, method 7, is adopted for the baseline. The following Results Section will examine the velocity space from the particles produced from these baseline ionization methods in order to probe the physics of ion motion with respect to nonthermal atmospheric loss.

4. Results

[28] Figures 3–8 illustrate O^+ fluxes from a virtual detector as a function of energy and production mechanism. The virtual detectors built into the MTP simulation focus on three radial directions around Mars: downtail, the northern pole, and the southern pole. Specifically, the downtail location is in the equatorial plane directly behind the planet (180° away from the Sun). The north and south pole locations are in the terminator plane directly above and below the planet, respectively. As discussed in the previous section, the baseline for O^+ ionization in the following plots will include photoionization using an optical shadow, charge exchange as a function of the total velocity (as seen in equation (9)), and temperature-dependent electron impact (methods 2, 5, and 7). The results are for a specific IMF orientation (away sector Parker spiral) and would largely be reversed for an opposite IMF, where features in the northern hemisphere would occur in the southern hemisphere. However, features due to the crustal magnetic field would not be reversed.

4.1. Downtail

[29] Beginning with the downtail location, Figure 3 is a logarithmic comparison of flux versus energy in keV in units of number per cm^2 per second per steradian. In Figure 3a,
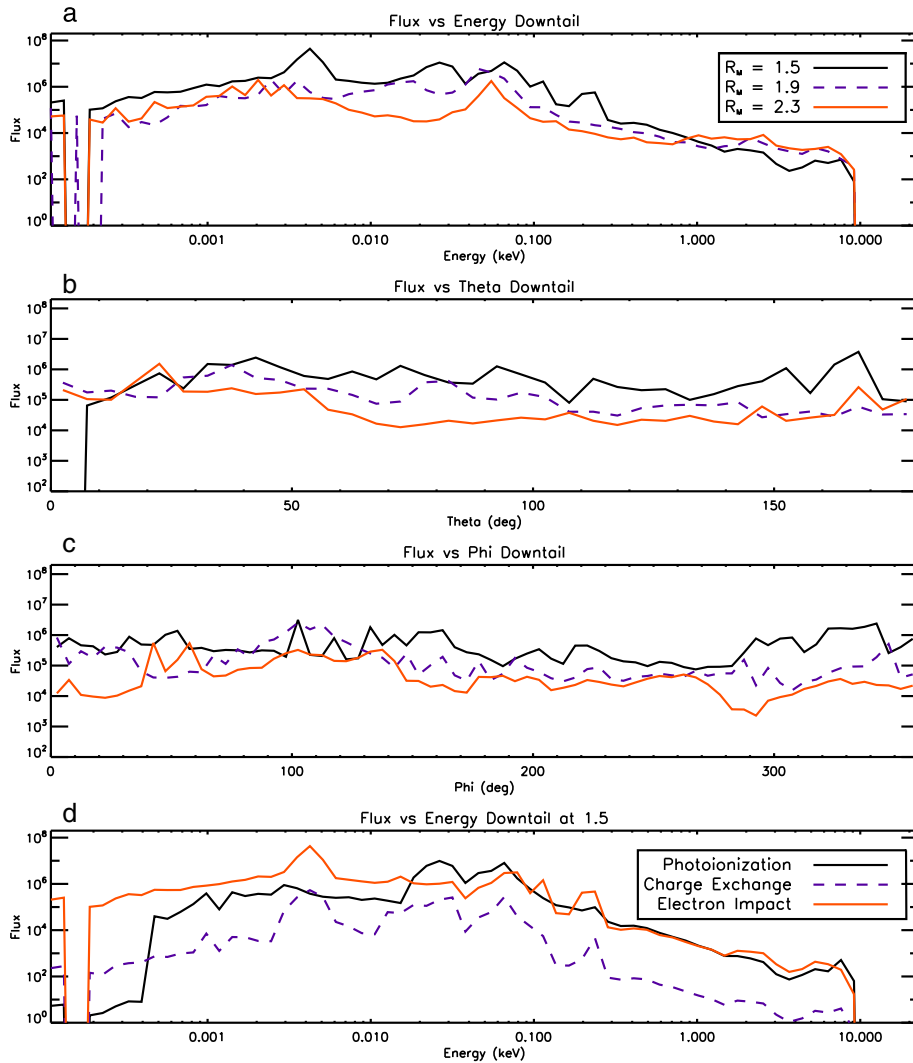
Figure 3. Three panels illustrate different fluxes as a function of energy at 1.5 and 2.5 R_M downtail. (a) Logarithmic comparison of flux versus energy in keV. (b) and (c) Flux versus energy plot is broken down into the ionization sources at 1.5 and 2.5 R_M downtail.
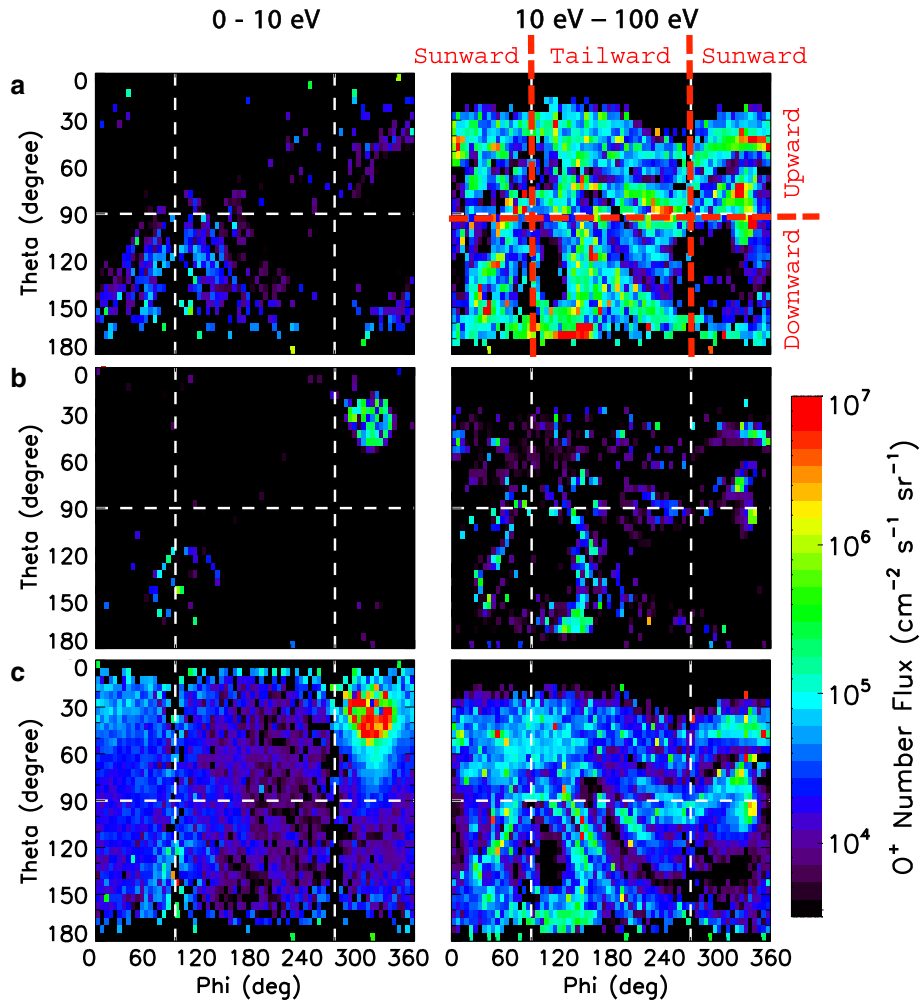
Figure 4. Velocity space distributions from a virtual detector downtail illustrating the contribution of different ionization source mechanisms and different energy levels at 1.5 R_M. Theta is the polar angle where $0° < \theta < 90°$ represents upward velocity and phi is the azimuthal angle where $90° < \varphi < 270°$ represents tailward motion and $0° < \varphi < 90°$ and $270° < \varphi < 360°$ correspond to a sunward motion. (a) Photoionization, (b) charge exchange, and (c) electron impact. The energy ranges are from 0–10 eV and 10–100 eV.

the virtual detectors are located at 1.5 and 2.5 R_M, as seen by the black and red lines, respectively.

[30] The higher flux peaks at 1.5 R_M, versus 2.5 R_M, represent the more turbulent environment inside of the induced magnetosheath. Because the IMF is draped around the planet, the field lines are stretched tailward and a current sheet is created, which accelerates the ions [see Nagy et al., 2004, Figure 4.7]. At 1.5 R_M in Figure 3a, peaks can be seen around 4 eV and again between 10 and 100 eV (solid black line). Figure 3b decomposes the flux at 1.5 R_M into the contributions of the baseline ionization mechanisms. The first peak at 4 eV is dominated by electron impact (pink line) while the peaks between 10 to 100 eV are dominated by photoionization (blue line). As seen in Figure 1g, there is local electron impact production downtail while Figure 1b shows that there is no photoionization production in the tail region due to the optical shadow. Thus, any flux from photoionization has been transported and reaches medium energies (the 10 to 100 eV peaks) while the locally produced electron impact flux has a lower energy peak (4 eV). In Figure 3c at

2.5 R_M, there is less flux below 1 keV than at 1.5 R_M because there are less locally produced ions. At > 1 keV, the flux is higher than at 1.5 R_M because ions are transported and accelerated downtail.

[31] The simulated downtail fluxes in Figure 3 show agreement with ASPERA-3 measurements. The simulated average and peak fluxes integrated over all energies at 1.5 R_M are 2.3×10^6 and 4.4×10^7 cm^2 s^{-1}, respectively. Barabash et al. [2007] reported average fluxes of O$^+$ in the downtail plasma sheet region of $\sim 2 \times 10^6$ cm^2 s^{-1} and peak fluxes of 5×10^7.

[32] While the fluxes at different energies in Figure 3 illustrate which ionization mechanisms are dominant, a valuable aspect of test particle simulations is the ability to resolve individual ion trajectories. Figure 4 illustrates a modified velocity space distribution (VSD) as a function of O$^+$ flight angle in the downtail region. The x-axis uses the azimuthal angle for the ions' flight direction. It is measured from the + X axis in the X-Y plane where $90° < \varphi < 270°$ represents tailward motion and $0° < \varphi < 90°$ or $270° < \varphi < 360°$
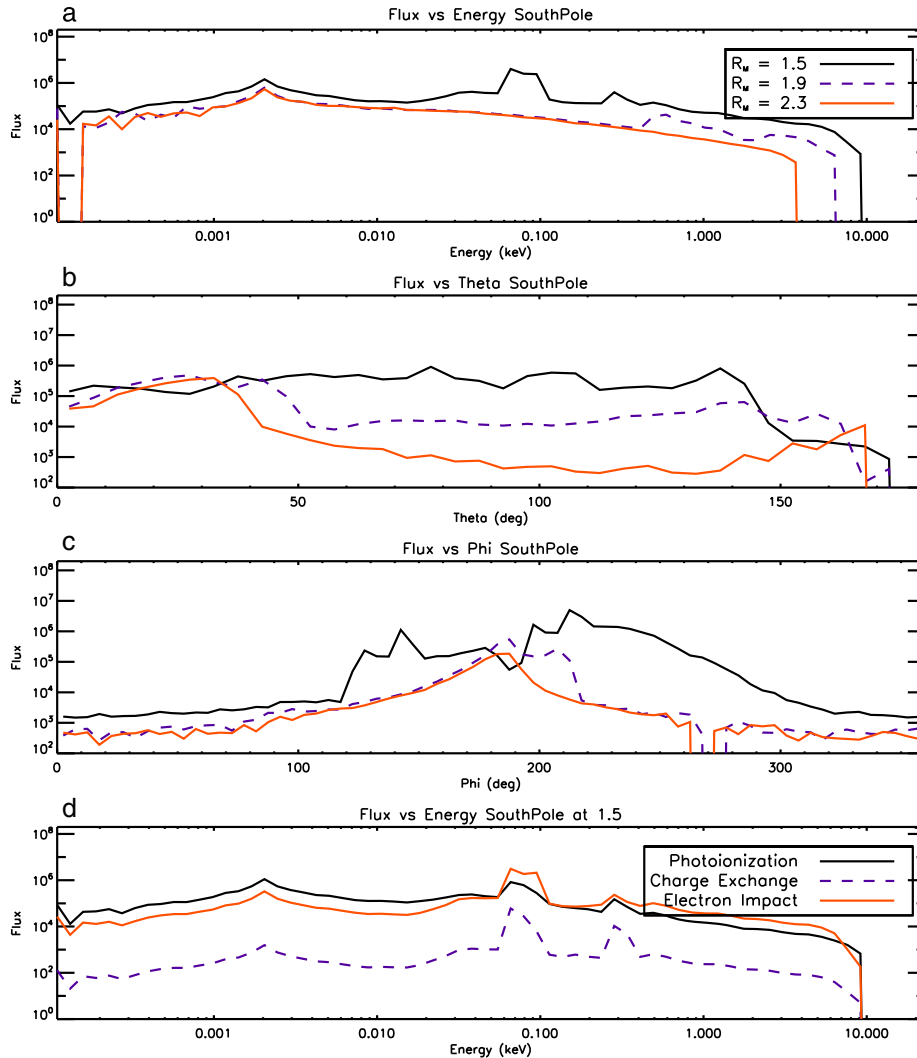
Figure 5. Three panels illustrate different fluxes as a function of energy at 1.5 and 2.5 R_M in the south pole. (a) Logarithmic comparison of flux versus energy in keV. (b) and (c) Flux versus energy plot is broken down into the ionization sources at 1.5 and 2.5 R_M in the south pole.

corresponds to a sunward motion. The *y*-axis uses the polar angle measured from the $+Z$ axis where $0° < \theta < 90°$ represents upward motion and $90° < \theta < 180°$ represents downward motion (see red dashed overlay). The color bar represents the flux in units of number per cm^2 per second per steradian as seen in the flux versus energy plots.

[33] Figure 4 shows the three ionization sources at 1.5 R_M downtail: (a) photoionization, (b) charge exchange, and (c) electron impact. The velocity space is integrated over two energy ranges (low = 0–10 eV, medium = 10–100 eV). As seen in the Figure 3b energy versus flux plots, electron impact dominates the low energy range with a peak at 4 eV while photoionization is dominant in the medium energy range from 20 to 100 eV. Not only does Figure 4 reflect this but the VSDs show two distinct ion populations: the low energy range contains an electron impact population moving upward and sunward (Figure 4c, 0–10 eV) while the medium energy range has asymmetric filamental structures due to photoionization moving downward (Figure 4a, 10–100 eV). At 1.5 R_M, the particles are within the magnetotail and are shielded from the strong convective electric field from the

solar wind and consequently have varying angles due to the bounce around the strong magnetic field, as seen in both low and medium ion populations.

4.2. South Pole

[34] In examining flux versus energy at the southern pole locations in Figure 5, the same pattern for higher fluxes within the magnetosheath exists. The line plots are much smoother in the south pole due to the lack of turbulence along the draped IMF field lines (relative to the tail region) and the peak flux is about an order of magnitude less than those fluxes downtail. The ions produced in the south pole either precipitate back into the atmosphere due to the convective electric field pointing into the planet or accelerate past the planet and are transported downtail. Figure 5a at 1.5 R_M (solid black line) illustrates a strong peak around 80–100 eV, which dominates the energy versus flux signature, discussed in terms of velocity space further down. A particular point of interest in Figure 5a is the high energy "cutoff"; at 1.5 R_M (black line), the flux does not exceed 9.5 keV, but only reaches 2.6 keV at 2.5 R_M (red line). This
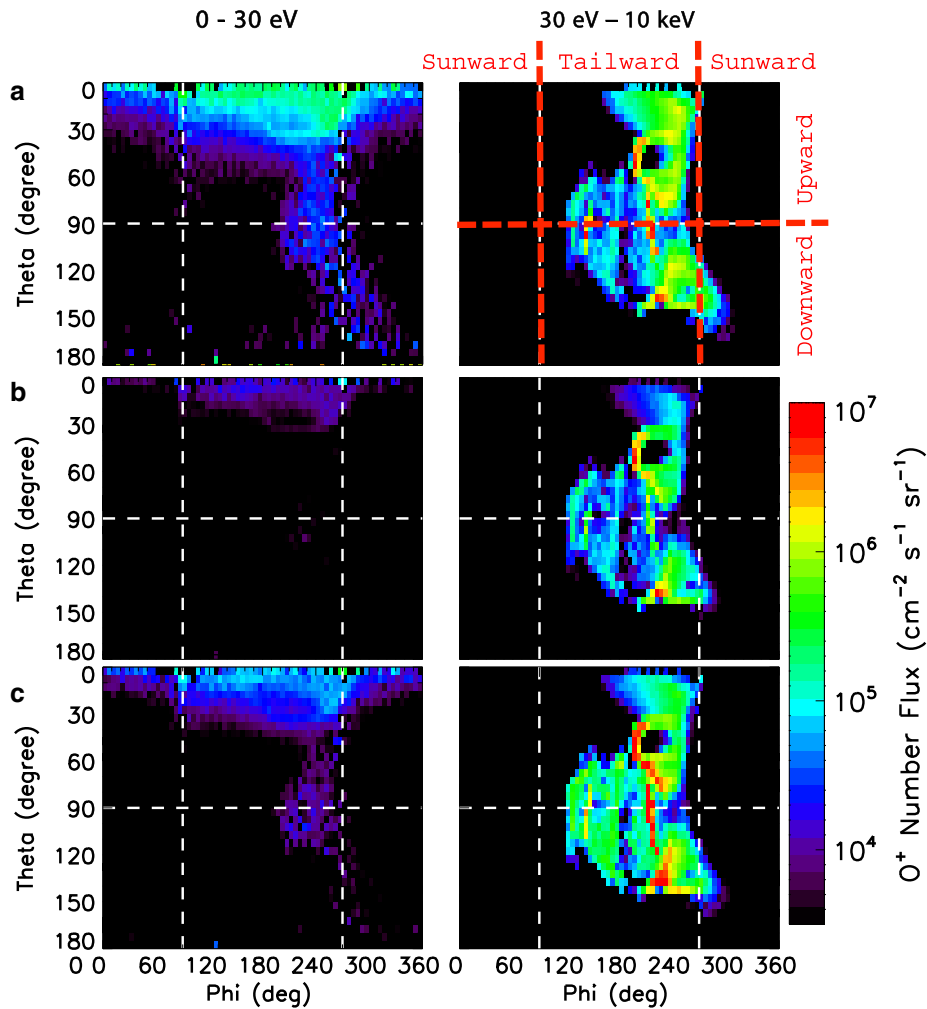
Figure 6. Velocity space distributions from a virtual detector over the south pole illustrating distinct populations of O$^+$ at 1.5 R_M. (a) Photoionization, (b) charge exchange, and (c) electron impact. The energy ranges are from 0–30 eV and 30 eV to 10 keV.

lower energy cutoff at higher altitudes is due to a shorter ion trajectory from its place of origin to the detector. Recall from Figure 1g that electron impaction ionization has relatively high O$^+$ production in the terminator plane between 1.5 and 2.5 R_M. Because the convective electric field points into the planet (for this IMF configuration), ions produced between 2.5 R_M and the bow shock would not have time to accelerate before hitting the detector at 2.5 R_M. However, they are accelerated for longer distances to the virtual detector at 1.5 R_M and thus have higher energies (the path length is larger when integrating $E \cdot dl$).

[35] Figures 5b and 5c break the ionization sources down at 1.5 and 2.5 R_M. Figure 5b illustrates that below 100 eV at 1.5 R_M photoionization is dominant because the O$^+$ ions are locally produced and the detector is no longer in the optical shadow. Above 100 eV, O$^+$ ions produced from electron impact in the terminator plane (again, see Figure 1g) are transported and swept toward the planet due to the convective electric field. In Figure 5c the detector is placed further from the planet at 2.5 R_M, but in a much higher area of electron impact production. Here the locally produced electron impact ions dominate the O$^+$ flux.

[36] Expanding on the Figure 5 dominant peaks, Figure 6 shows VSDs when the detectors are positioned in the southern pole at 1.5 R_M. Figure 6a is photoionization, Figure 6b is charge exchange, and Figure 6c is electron impact. The velocity space is integrated over two energy ranges (low = 0–30 eV, high = 30 eV to 10 keV). Figure 6a illustrates that photoionization dominates the 0–30 eV energies with more upward and tailward flux, corresponding to the 2 eV peak from Figure 5b. At the higher energies of 30 eV to 10 keV, all three sources look similar except in Figure 6c where the electron impact VSD has higher flux (red filamental structure at $\varphi = \sim 190°$ and $\theta = \sim 90°$) which corresponds to the 100 eV peak from Figure 5b. Thus, Figure 6 illustrates distinct ion populations—low energy photoionization ions which were locally produced and electron impact ions which were created at the terminator and accelerated to higher energies under the planet.

4.3. North Pole: Polar Features

[37] Figure 7 illustrates flux versus energy in the northern pole location and highlights the northern polar plume, a phenomenon that has been predicted by numerous models
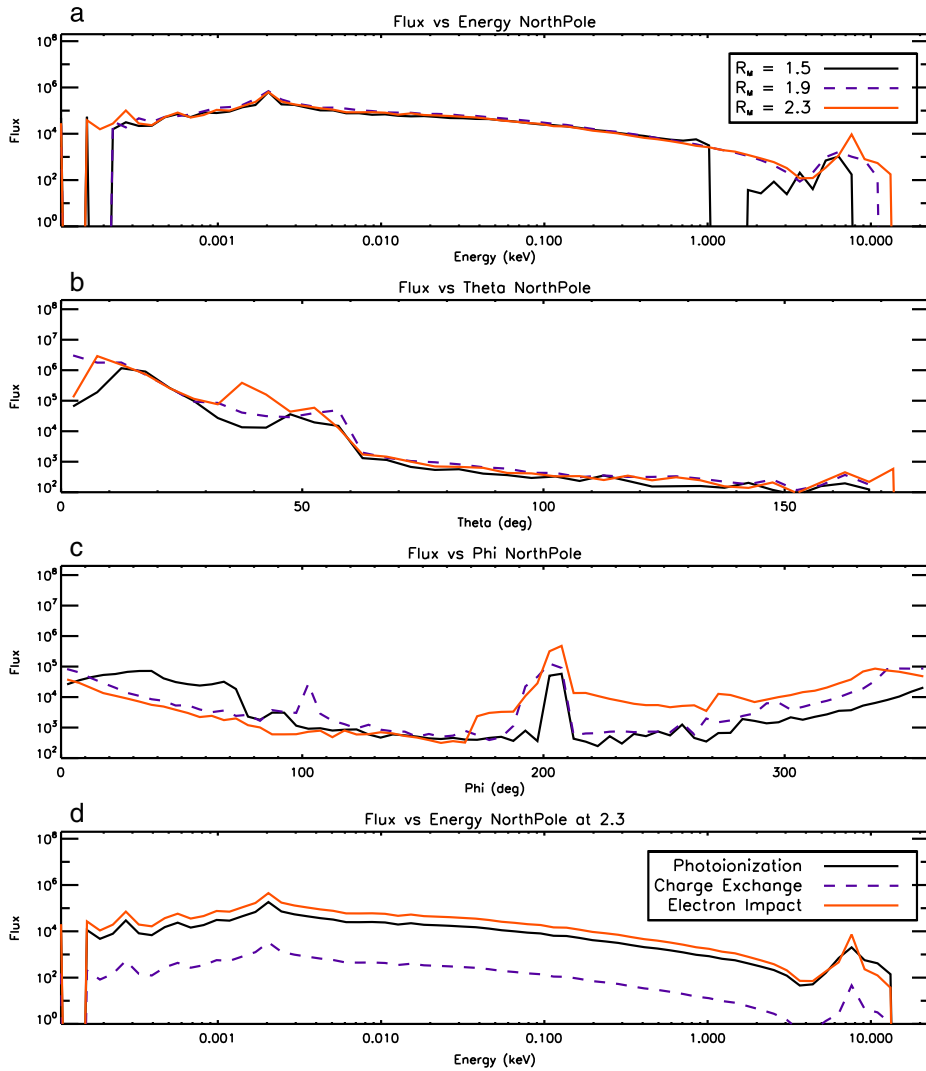
Figure 7. Three panels illustrate different fluxes as a function of energy at 1.5 and 2.5 R_M at the north pole. (a) Logarithmic comparison of flux versus energy in keV. (b) and (c) Flux versus energy plot is broken down into the ionization sources at 1.5 and 2.5 R_M at the north pole.

but is yet to be observed [*Brecht and Ledvina*, 2006; *Fang et al.*, 2008, 2010; *Najib et al.*, 2011]. The magnitude of the flux is the lowest here compared to the downtail and south pole regions but is also the smoothest and depicts a clear track for ion acceleration. In Figure 7a, the sharp peak in the 3 to 20 keV range illustrates an O^+ polar plume at both 1.5 and 2.5 R_M. Figure 7b shows that the polar plume at 1.5 R_M is marginally dominated by photoionization. At 2.5 R_M, Figure 7c illustrates that the flux is marginally dominated by electron impact, but clearly all of the ions regardless of their ionization source have been accelerated straight upward to high energies.

[38] In Figure 8, the velocity space signature is shown for the north pole at 1.5 R_M where Figure 8a is photoionization, Figure 8b is charge exchange, and Figure 8c is electron impact. The velocity space is integrated over two energy ranges (low = 0–100 eV, high = 100 eV to 25 keV). The low energy range includes the 2 eV peak seen in the line plots of Figure 7 and represents the locally produced ions. The higher energy range captures the sharp peak from 1 to 25 keV, displaying a

plume structure moving directly upward, slightly dominated by photoionization. For this IMF configuration, ions are created on the dayside by photoionization, charge exchange and electron impact and are accelerated relatively evenly directly above the planet.

5. Escape

[39] Figure 9 illustrates that the spatial distribution of O^+ escape through a 3 R_M shell. As previously discussed, the simulation domain uses a coordinate system that corresponds to MSO directions and the escape shown is for an IMF with an away sector Parker spiral configuration. The northern and southern hemisphere loss shells are shown for each baseline ionization source (top and bottom, respectively). Note that the view is from over the north pole for all of the panels with the Sun to the right. The loss is calculated by recording a particle as it passes through the 3 R_M spherical boundary and weighting it. As described earlier, the weight is determined by the total ion production per cell
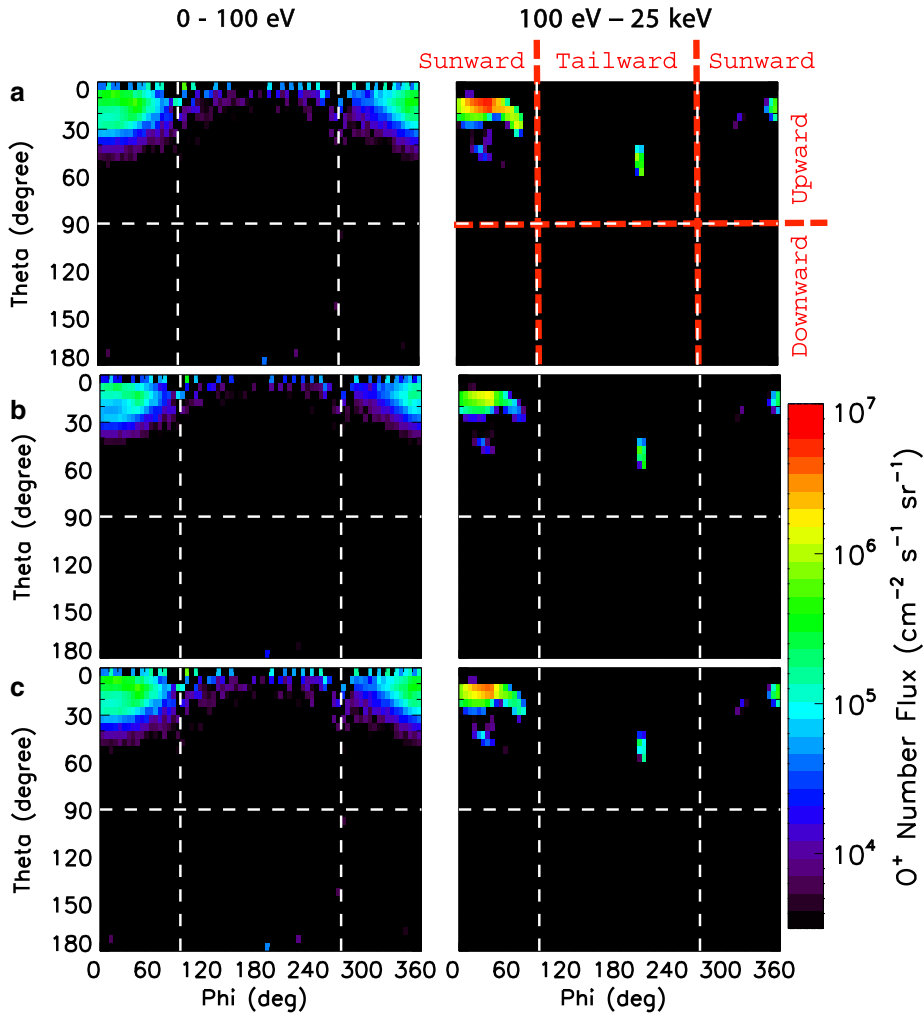
Figure 8. Velocity space distributions from a virtual detector over the north pole illustrating a concentrated plume of O$^+$ at 1.5 R_M. (a) Photoionization, (b) is charge exchange, and (c) electron impact. The energy ranges are from 0–100 eV and 100 eV to 25 keV.

divided by the total number of test particles per unit time [*Fang et al.*, 2008]. The color bar is a log scale of the flux in # cm^{-2} s^{-1}.

[40] The loss shells of O$^+$ from Figure 9 clearly show a northern polar plume, which is in agreement with particle traces performed by *Fang et al.* [2008, 2010]. In the northern hemispheric loss shell, all three sources have the peak of the northern polar plume slightly sunward and display a fan of tailward loss. The northern polar plume is a result of the background convective electric field with a strong $+Z_{MSO}$ component. The southern hemisphere displays very little escape because the O$^+$ ions have been accelerated upward and tailward by the strong convective electric field. In the tail regions ($-X_{MSO}$ plane) of Figure 9, loss from photoionization and charge exchange display two separate fans on each side of the $Y_{MSO} = 0$ plane. However, electron impact ions lost through the 3 R_M shell appear to form one major stream in just the $+Y_{MSO}$ quadrant. These different tails illustrate the asymmetry that exists in the dawn-dusk direction. As a result of the Parker spiral, the E × B drift from the IMF accelerates the particles in the $-Y_{MSO}$ direction so there would be an expected increase in loss on the dawn side.

[41] The O$^+$ escape signatures seen in Figure 9 are in agreement with other modeling efforts and observations. The dawn-dusk asymmetry has been observed with particle traces by *Fang et al.* [2008], hybrid models [*Kallio and Jarvinen*, 2012] and observations [*Dubinin et al.*, 2006]. The preferential loss in the northern hemisphere has been reported by *Brecht and Ledvina* [2010] who noted in particular that the crustal fields in the southern hemisphere are correlated with slower ion pick up as a result of the parallel electric fields. Additionally, *Lundin et al.* [2011] found that the averaged flux flow directions measured from ASPERA-3 suggested that the crustal fields reduced tailward transport of O$^+$ and as a consequence reduced escape over the southern hemisphere. Finally, the northern polar plume has been predicted in both MHD and hybrid models [*Brecht and Ledvina*, 2006; *Fang et al.*, 2008, 2010; *Najib et al.*, 2011].

[42] The plots of flux distributions and escape (Figures 3–9) thus far have presented one O$^+$ production baseline in order to highlight their influence on ion trajectories. However, the method of ion production plays a critical role in total escape. Table 2 presents the production and loss rate contributions for each method in #/sec. The production rate is the product of
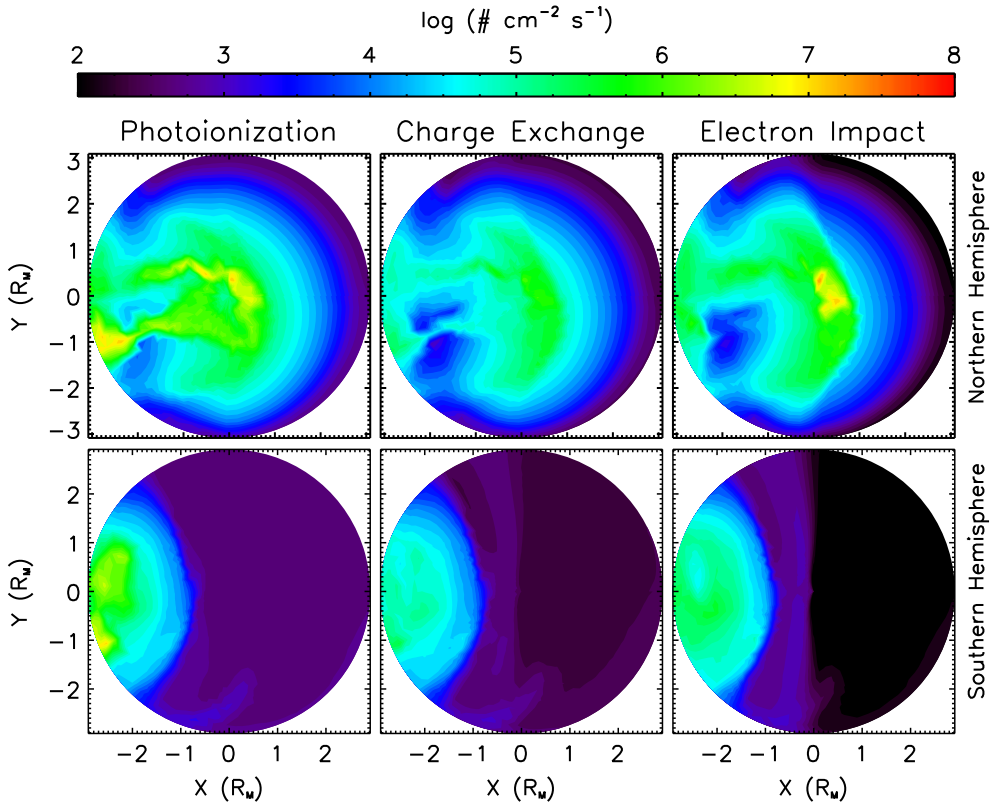
Figure 9. The escape of O^+ from the three source regions at the outer boundary shell of 3 R_M in the northern and southern hemisphere with the Sun to the right. The view for both hemispheres is from over the north pole and the color bar is in units of $cm^{-2} s^{-1}$.

Table 2. O^+ Production and Loss as a Function of Reaction Rates (#/s).

#	Method	Production Rates	Escape Rate	% Efficiency
1	Photoionization[a]	1.2×10^{25}	2.8×10^{24}	23.3
2	Photoionization[b]	1.8×10^{25}	3.8×10^{24}	21.1
3	Charge exchange[c]	6.4×10^{23}	1.0×10^{23}	15.6
4	Charge exchange[d]	3.5×10^{25}	6.2×10^{24}	17.7
5	Charge exchange[e]	1.2×10^{24}	5.5×10^{23}	45.8
6	Electron impact[f]	1.2×10^{27}	1.6×10^{26}	13.3
7	Electron impact[g]	5.6×10^{24}	2.0×10^{24}	35.7

[a]Photoionization using solar zenith angle.
[b]Photoionization using an optical shadow.
[c]Charge exchange constant used by *Ma et al.* [2004] (cold H^+ + O).
[d]Charge exchange constant used by *Stebbings et al.* [1964] with upstream bulk velocity (hot H^+ + O).
[e]Charge exchange using bulk and random velocity (hot H^+ + O).
[f]Electron impact using constant temperature of 1.5×10^5 K.
[g]Electron impact using calculated electron temperature per cell.

the atmospheric density, the reaction rate and the volume. The loss rate is the escaping flux integrated over the 3 R_M shell, seen in Figure 9. We define the efficiency as the ratio of the loss rate to the production rate, illustrating how effectively O^+ ions are produced and retained in the Mars space environment for each ionization mechanism. High efficiency would correspond to a higher loss fraction per unit of production, meaning ions are more likely to escape through the 3 R_M shell. Similarly, a low efficiency ratio would suggest that the ions are less likely to escape.

[43] Table 2 begins with comparing photoionization using solar zenith angle dependence (method 1) and photoionization using an optical shadow (method 2). Method (1) has lower production and loss but has a very similar efficiency ratio as method (2). Ultimately, using photoionization with an optical shadow (2) produces more O^+ ions, but a smaller percentage are lost outside of the 3 R_M shell.

[44] Following, Table 2 compares charge exchange with three methods: a constant reaction rate consistent with *Ma et al.* [2004] based on cold ions and neutrals (method 3), a bulk velocity based constant reaction rate which is consistent with *Stebbings et al.* [1964] (method 4), and finally a novel method dependent on the bulk and random velocity (method 5). Methods 3, 4, and 5 have more than an order of magnitude difference in both production and loss rates based on their physical assumptions. Method 3 has smaller production and escape rates due to only accounting for cold ion neutral collisions and ignoring the hot solar wind ion collisions with the corona. Method 4 has the largest rates because it overestimates the production by assuming the solar wind flow has the same velocity throughout the simulation. Note that methods 3 and 4 have similar efficiency ratios which are quite low; this suggests that the O^+ ions produced from these methods are much less likely to escape from the 3 R_M shell. Method 5 however has production and loss rates in between methods 3 and 4, but has the highest efficiency ratio of 45.8%. Using this scheme, almost half the O^+ ions produced are likely to escape.

[45] Finally, Table 2 compares the electron impact with a constant temperature reaction rate (method 6) and a temperature-dependent reaction rate (method 7). Method (6) yields the highest rate of production and loss rates by two orders of magnitude. As discussed in Figure 2, at altitudes below 1.3 R_M (< 1000 km), the same reaction rate is applied to the dense neutral atmosphere which creates an enormous amount of O^+ ions. Due to this large production rate, the efficiency ratio is the smallest, 13.3%, because most of these ions are produced at low altitudes and do not get accelerated away from the planet and are unlikely to escape from the 3 R_M shell. The final method, the temperature-dependent electron impact ionization (7), has a much smaller reaction rate at the low altitudes, as seen in Figure 2. Consequently, it has a much smaller O^+ production rate. But method 7 also has a higher efficiency ratio which suggests that ions produced from an electron temperature-dependent reaction rate are more likely to escape from the 3 R_M shell.

6. Discussion

[46] Numerous simulations have been used to investigate the subject of nonthermal atmospheric escape in order to assess the broader context of atmospheric evolution on Mars. Over an order of magnitude difference in the net O^+ loss estimates exist among observations and simulations [*Stebbings et al.*, 1964; *Zhang et al.*, 1993; *Bauske et al.*, 1998; *Ma et al.*, 2004; *Modolo et al.*, 2005; *Brecht and Ledvina*, 2006; *Barabash et al.*, 2007; *Fang et al.*, 2008; *Kaneda et al.*, 2009; *Terada et al.*, 2009; *Brain et al.*, 2010; *Lundin et al.*, 2011; *Najib et al.*, 2011], providing a strong incentive to probe the assumptions and physics that influence loss. This study examines the influencing factors on the escape rate of O^+ by comparing ion production mechanisms and their effect on production, escape and velocity space in the Mars space environment.

[47] Before discussing the results, a review of the model's assumptions, limitations and inputs is valuable. First, it is important to note that when O^+ densities become larger than the background MHD solar wind density, the plasma pressure balance and species weighted velocity would shift and consequently the static field assumptions of the MTP, or any test particle simulation, would no longer be appropriate due to the lack of self-consistency. As long as the MTP plasma environment can remain static and collisionless, this model serves as an excellent tool for probing pickup ion motion and escape. The MTP finds O^+ number densities consistent with the MHD ion density profiles except at the North Pole where the plume redirects a significant population of O^+. However, even here, the O^+ densities are two orders of magnitude smaller than the solar wind protons and therefore the test particle assumption is still valid. The MTP O^+ velocities are also consistent with the MHD bulk velocity except for acceleration of the O^+ ions to higher energies focused in center of the tail. Because the MTP accelerated downtail ion velocity is in the same direction as the MHD bulk velocity, both of which are below 50 km/s, there would not be a significant change in the MHD fields. In addition to the static field assumptions, the inputs for all of the production and loss calculations were done for a single realization of solar EUV and solar wind and IMF conditions. The specific configuration is with solar maximum conditions, slow solar wind, and away sector Parker spiral IMF. For example, if the IMF was reversed (in the toward sector), the northern polar plume would in fact occur over the southern pole.

[48] Using identical inputs, the section 3 began with assessing each source method and comparing their physical assumptions against one another, as seen in Table 1 and illustrated in Figure 1. First, photoionization was compared as a function of solar zenith angle (method 1) and optical shadow (method 2), producing similar production and loss rates. Photoionization using an optical shadow was adopted as a baseline due to the atmosphere being optically thin in the simulation space (300 km and above). The three methods examined for O^+ production via charge exchange varied much more so, spanning over two orders of magnitude. The rate used by *Ma et al.* [2004] was derived from *Fox and Sung* [2001], which assumed cold ion and neutral collisions (method 3). The *Stebbings et al.* [1964] production scheme accounted for the hot ion collisions (hot energetic charge exchange) by using production rates as a function of the oxygen cross-section and solar wind bulk velocity (method 4). Finally, this study expanded on the hot energetic charge exchange approach and used the same cross section but with the total velocity consisting of the random and bulk velocity (method 5), as seen in equation (9). Method 5 was included in the baseline because it takes into account the hot ion collisions while incorporating the changes in solar wind velocity near a planetary obstacle. The authors stress the novelty of this approach because of its physically based relevance as well as its influence on O^+ escape. Finally, electron impact ionization was considered as a constant with $T_e = 1.5 \times 10^5$ K (method 6) and as function of electron temperature dependence (method 7). As seen in Figure 2, using a reaction rate with temperature dependence does not overestimate the production at lower altitudes (< 1000 km), and is therefore adopted into the baseline.

[49] In section 4, virtual detectors were placed at 1.5 and 2.5 R_M in three locations in the simulation space: downtail, the south pole and the north pole. The flux versus energy plots and VSDs, Figures 3–8 illustrate independent ion populations at different energies for each baseline production mechanism. Downtail, the virtual detector is in the optical shadow. The lower energy ion populations are indicative of locally produced electron impact ions while the higher energies are dominated by transported photoionization ions. Peak and average fluxes over all energies show agreement with both *Barabash et al.* [2007] and *Lundin et al.* [2011]. In the south pole, the virtual detector is outside of the optical shadow and locally produced photoionization ions dominate the low energy ions. At higher energies in the south pole, electron impact ions dominate because they are transported from high production in the terminator toward the planet by the background convective electric field. The northern pole exhibits a clear polar plume at all altitudes with energies of 4 keV and higher regardless of the source.

[50] Section 5 illustrates the escape shells at 3 R_M for each baseline production mechanism in Figure 9. Due to the northern polar plume, there is a preferential northern hemispheric loss for this specific IMF configuration (away sector Parker spiral). Each of the ionization mechanisms also exhibit different spatial channels as a result of where the ions were produced and accelerated. Accordingly, future satellite missions might further investigate the spatial distribution of

ion loss for orbital considerations. Finally in Table 2, the production and loss rates (# s^{-1}) are presented along with their ratio. Considering only the baseline production mechanisms (methods 2, 5, and 7), the O$^+$ escape (# sec^{-1}) is estimated to be 3.8×10^{24} for photoionization, 5.5×10^{23} for charge exchange and 2.0×10^{24} for electron impact, resulting in a net loss of 6.4×10^{24}.

7. Summary

[51] The MTP model provides a unique and valuable approach for studying the various physical processes controlling O$^+$ ion creation, transport, and loss through near-Mars space. The resolution provided by over four billion test particles permits the examination of pick-up ion flux distributions in spatial locations and energy ranges that have not been examined before. Because the MTP simulation does not average the gyroradii or pitch angles, it can account for ions on an unmagnetized planet with gyroradii on planetary scales.

[52] This study has demonstrated the importance of the ion production mechanisms and their effect on velocity space and total O$^+$ ion escape by probing the physical assumptions of O$^+$ ion creation. In particular we found three unique results: (1) The use of a photoionization source with an optical shadow rather than a solar zenith angle dependence is an appropriate alternative for high altitude ion production. (2) There are several commonly used constants for the charge exchange production rate, which either neglect the hot solar wind ions interacting with the corona or do not account for the variable velocity as the solar wind approaches the planetary obstacle. A new charge exchange cross section has been introduced that is dependent on the total proton speed (bulk plus random velocity). (3) Because the electron impact ionization rate is highly dependent on temperature, a constant electron impact reaction rate drastically overestimates the low altitude O$^+$ ion production (<1000 km). Thus, the use of a temperature-dependent rate is critical to physically model ionization at all altitudes.

[53] The authors encourage MHD, hybrid and test particle simulations to explore these ionization mechanisms and stress this study is meant to be an aid for models and simulations in the broader context of examining atmospheric escape. Future work will include following the trajectories of additional species, including a source of ionospheric outflow, and providing data comparisons with ions in the Mars plasma environment.

References

Acuna, M. H., et al. (1999). Global distribution of crustal magnetization discovered by the Mars global surveyor MAG/ER experiment, *Science*, *284*(5415), 790–793.

Andersson, L., R. E. Ergun, and A. I. F. Stewart. (2010). The combined atmospheric photochemistry and ion tracing code: Reproducing the Viking lander results and initial outflow results, *Icarus*, *206*(1), 120–129.

Arkani-Hamed, J. (2001). A 50-degree spherical harmonic model of the magnetic field of Mars, *J. Geophys. Res.*, *106*, 197–208.

Barabash, S., E. Dubinin, N. Pissarenko, R. Lundin, and C. T. Russell. (1991). Picked up protons near Mars: Phobos observations, *Geophys. Res. Lett.*, *18*(10), 1805–1808.

Barabash, S., A. Fedorov, R. Lundin, and J. A. Sauvaud. (2007). Martian atmospheric erosion rates, *Science*, *315*(5811), 501–3.

Bauske, R., A. Nagy, T. Gombosi, D. De Zeeuw, K. Powell, and J. Luhmann. (1998). A three-dimensional MHD study of solar wind mass loading processes at Venus: Effects of photoionization, electron impact ionization, and charge exchange, *J. Geophys. Res.*, *103*(A10), 625–638.

Boesswetter, A., et al. (2007). Comparison of plasma data from Aspera-3/Mars-Express with a 3-D hybrid simulation, *Ann. Geophys.*, *25*, 1851–1864.

Bougher, S. W., and S. Engel. (2000). Comparative terrestrial planet thermospheres: 3. Solar cycle variation of global structure and winds at solstices, *J. Geophys. Res.*, *105*, 669–692.

Brain, D., et al. (2010). A comparison of global models for the solar wind interaction with Mars, *Icarus*, *206*(1), 139–151.

Brecht, S. H., and S. A. Ledvina. (2006). The solar wind interaction with the Martian ionosphere/atmosphere, *Space Sci. Rev.*, *126*(1-4), 15–38.

Brecht, S. H., and S. A. Ledvina. (2010). The loss of water from Mars: Numerical results and challenges, *Icarus*, *206*(1), 164–173.

Carr, M. H. (2003). Oceans on Mars: An assessment of the observational evidence and possible fate, *J. Geophys. Res.*, *108*(E5).

Chaufray, J. Y., R. Modolo, F. Leblanc, G. Chanteur, R. E. Johnson, and J. G. Luhmann. (2007). Mars solar wind interaction: Formation of the Martian corona and atmospheric loss to space, *J. Geophys. Res.*, *112*(E9).

Cravens, T. E., J. U. Kozyra, A. Nagy, T. Gombosi, and M. Kurtz. (1987). Electron impact ionization in the vicinity of comets, *J. Geophys. Res.*, *92*, 7341–7353.

Cravens, T. E., A. Hoppe, and S. A. Ledvina. (2002). Pickup ions near Mars associated with escaping oxygen atoms, *J. Geophys. Res.*, *107*(A8), 1170–1180.

Dubinin, E., M. Frnz, J. Woch, E. Roussos, S. Barabash, R. Lundin, J. D. Winningham, R. A. Frahm, and M. Acua. (2006). Plasma morphology at Mars. ASPERA-3 observations, *Space Sci. Rev.*, *126*(1-4), 209–238.

Fang, X., M. W. Liemohn, A. F. Nagy, Y. Ma, D. L. De Zeeuw, J. U. Kozyra, and T. H. Zurbuchen. (2008). Pickup oxygen ion velocity space and spatial distribution around Mars, *J. Geophys. Res.*, *113*(A2).

Fang, X., M. W. Liemohn, A. F. Nagy, J. G. Luhmann, and Y. Ma. (2010). On the effect of the Martian crustal magnetic field on atmospheric erosion, *Icarus*, *206*(1), 130–138.

Fedorov, A., et al. (2006). Structure of the Martian wake, *Icarus*, *182*(2), 329–336.

Fox, J. L. (1993). On the escape of oxygen and hydrogen from Mars, *Geophys. Res. Lett.*, *20*(17), 1847–1850.

Fox, J. L. (2003). Effect of H$_2$ on the Martian ionosphere: Implications for atmospheric evolution, *J. Geophys. Res.*, *108*(A6).

Fox, J. L., and K. Sung. (2001). Solar activity variations of the Venus thermosphere/ionosphere, *J. Geophys. Res.*, *106*, 305–335.

Harnett, E. M., and R. M. Winglee. (2006). Three-dimensional multifluid simulations of ionospheric loss at Mars from nominal solar wind conditions to magnetic cloud events, *J. Geophys. Res.*, *111*(A9).

Hunten, D. M. (1993). Atmospheric evolution of the terrestrial planets, *Science*, *259*(5097), 915–920.

Jin, H., K. Maezawa, and T. Mukai. (2006). Effects of charge exchange and electron impact ionization on the formation of the magnetic pileup boundary at Mars, *J. Geophys. Res.*, *111*(A5).

Johnson, R. E. (1994). Plasma-induced sputtering of an atmosphere, *Space Sci. Rev.*, *69*(3-4), 215–253.

Kallio, E., and R. Jarvinen. (2012). Kinetic effects on ion escape at Mars and Venus: Hybrid modeling studies, *Earth Planet. Space*, *64*(2), 157–163.

Kallio, E., and H. Koskinen. (1999). A test particle simulation of the motion of oxygen ions and solar wind protons near Mars, *J. Geophys. Res.*, *104* (A1), 557–579.

Kallio, E., K. Liu, R. Jarvinen, V. Pohjola, and P. Janhunen. (2010). Oxygen ion escape at Mars in a hybrid model: High energy and low energy ions, *Icarus*, *206*(1), 152–163.

Kaneda, K., N. Terada, and S. Machida. (2009). Solar-wind control of the hot oxygen corona around Mars, *J. Geophys. Res.*, *114*(E2).

Kim, J., A. Nagy, J. L. Fox, and T. E. Cravens. (1998). Solar cycle variability of hot oxygen atoms at Mars, *J. Geophys. Res.*, *103*, 339–342.

Lammer, H., and S. J. Bauer. (1991). Nonthermal atmospheric escape from Mars and Titan, *J. Geophys. Res.*, *96*(A2), 1819–1825.

Li, L., Y. Zhang, Y. Feng, X. Fang, and Y. Ma. (2011). Oxygen ion precipitation in the Martian atmosphere and its relation with the crustal magnetic fields, *J. Geophys. Res.*, *116*(A8).

Lichtenegger, H. I. M., H. Lammer, Y. N. Kulikov, S. Kazeminejad, G. H. Molina-Cuberos, R. Rodrigo, B. Kazeminejad, and G. Kirchengast.

(2007). Effects of low energetic neutral atoms on Martian and Venusian dayside exospheric temperature estimations, *Space Sci. Rev.*, *126*(1-4), 469–501.

Liu, Y., A. Nagy, C. Groth, D. De Zeeuw, T. Gombosi, and K. Powell. (1999). 3D multifluid MHD studies of the solar wind interaction with Mars, *Geophys. Res. Lett.*, *26*(17), 2689–2692.

Luhmann, J. G., and J. U. Kozyra. (1991). Dayside pickup oxygen ion precipitation at Venus and Mars spatial distributions energy deposition and consequences, *J. Geophys. Res.*, *96*, 5457–5467.

Luhmann, J. G., S. A. Ledvina, J. G. Lyon, and C. T. Russell. (2006). Venus O+ pickup ions: Collected PVO results and expectations for Venus Express, *Planet. Space Sci.*, *54*(13-14), 1457–1471.

Lundin, R., S. Barabash, M. Holmström, H. Nilsson, M. Yamauchi, E. M. Dubinin, and M. Fraenz. (2009). Atmospheric origin of cold ion escape from Mars, *Geophys. Res. Lett.*, *36*(17).

Lundin, R., S. Barabash, M. Yamauchi, H. Nilsson, and D. Brain. (2011). On the relation between plasma escape and the Martian crustal magnetic field, *Geophys. Res. Lett.*, *38*(2).

Lundin, R., et al. (1989). First measurements of the ionospheric plasma escape from Mars, *Nature*, *341*(6243), 609–612.

Lundin, R., et al. (2004). Solar wind-induced atmospheric erosion at Mars: first results from ASPERA-3 on Mars Express, *Science*, *305* (5692), 1933–6.

Ma, Y., A. Nagy, I. V. Sokolov, and K. C. Hansen. (2004). Three-dimensional, multispecies, high spatial resolution MHD studies of the solar wind interaction with Mars, *J. Geophys. Res.*, *109*(A7).

Ma, Y.-J., and A. F. Nagy. (2007). Ion escape fluxes from Mars, *Geophys. Res. Lett.*, *34*(8).

McKenna, L., E. Kallio, R. Jarvinen, and V. Afonin. (2012). Magnetic shadowing of high energy ions at Mars and how this effect can be simulated using a hybrid model, *Earth Planet. Space*, *64*(2), 247–256.

Modolo, R., G. Chanteur, E. Dubinin, and A. Matthews. (2005). Influence of the solar EUV flux on the Martian plasma environment, *Ann. Geophys.*, *23*, 433–444.

Nagy, A., et al. (2004). The plasma environment of Mars, *Space Sci. Rev.*, *111*, 33–114.

Najib, D., A. F. Nagy, G Toth, and Y. Ma. (2011). Three-dimensional, multifluid, high spatial resolution MHD model studies of the solar wind interaction with Mars, *J. Geophys. Res.*, *116*(A5).

Powell, K., P. Roe, T. Linde, T. Gombosi, and D. De Zeeuw. (1999). A solution-adaptive upwind scheme for ideal magnetohydrodynamics, *J. Comput. Phys.*, *154*, 284–309.

Rosenbauer, H., et al. (1989). Ions of Martian origin and plasma sheet in the Martian magnetosphere: initial results of the TAUS experiment, *Nature*, *341*(6243), 612–614.

Schunk, R., and A. Nagy. (2000). *Ionospheres*, Cambridge University Press, Cambridge.

Squyres, S. W., et al. (2004). In situ evidence for an ancient aqueous environment at Meridiani Planum, Mars, *Science*, *306*(5702), 1709–14.

Stebbings, R. F., A. C. H. Smith, and H. Ehrhardt. (1964). Charge transfer between oxygen atoms and O+ and H+ ions, *J. Geophys. Res.*, *69*(11), 2349–2355.

Terada, N., Y. N. Kulikov, H. Lammer, H. I. Lichtenegger, T. Tanaka, H. Shinagawa, and T. Zhang. (2009). Atmosphere and water loss from early Mars under extreme solar wind and extreme ultraviolet conditions, *Astrobiology*, *9*(1), 55–70.

Verigin, M. I., et al. (1991). On the problem of the Martian atmosphere dissipation: Phobos 2 TAUS spectrometer results, *J. Geophys. Res.*, *96* (A11), 19,315–19,320.

Zhang, M. H. G., J. Luhmann, A. Nagy, J. Spreiter, and S. Stahara. (1993). Oxygen ionization rates at Mars and Venus: Relative contributions of impact ionization and charge exchange, *J. Geophys. Res.*, *98*(2), 3311–3318.